Journal of
Materials Chemistry C

ROYAL SOCIETY
OF CHEMISTRY

PAPER

View Article Online
View Journal | View Issue

Published on 20 September 2021. Downloaded by HeFei University of Technology on 10/13/2022 3:39:42 AM.

Cite this: J. Mater. Chem. C, 2021, 9, 14897

Electrically adjusted deep-ultraviolet/near-infrared single-band/dual-band imaging photodetectors based on $Cs_3Cu_2I_5$/$PdTe_2$/Ge multiheterostructures†

Yi Liang,[a] Chao Xie, *[b] Cheng-yun Dong,[a] Xiao-wei Tong,[a] Wen-hua Yang,[b] Chun-yan Wu [a] and Lin-bao Luo *[a]

Received 9th September 2021,
Accepted 20th September 2021

DOI: 10.1039/d1tc04290d

rsc.li/materials-c

Multispectral photodetection has garnered enormous research interest and has always been challenging to date. Here, we present the realization of an electrically adjusted single-band/dual-band photodetector based on an inorganic lead-free halide $Cs_3Cu_2I_5$/two-dimensional (2D) $PdTe_2$ multilayer/Ge multiheterostructure. Owing to its unique optical property and distinct carrier transport behaviour, the device can be easily converted from a single-band photodetector operating in the near-infrared (NIR) region to a dual-band photodetector working in both deep-ultraviolet (DUV) and NIR regimes, upon applying a reverse bias voltage. Significantly, the device shows a peak responsivity of $\sim$694.1 mA W^{-1} at 1550 nm at zero bias, and maximum responsivity values of $\sim$744.2 mA W^{-1} and $\sim$712.5 mA W^{-1} at 265 nm and 1550 nm, respectively, at a small reverse bias. This characteristic also endows the photodetector with an excellent DUV/NIR dual-band optical imaging capability. This work will offer a new opportunity for designing high-performance photodetectors with multiple functionalities operating in complicated circumstances.

Introduction

Multispectral photodetectors can sense coincident spectral information *via* processing optical signals from multiple wavebands to supply better target recognition and to upgrade detection capacity in complicated environments.[1–3] High-performance multispectral photodetection is of paramount importance because of its wide military and civil applications in missile warning, optical guidance, third generation imaging, environment monitoring, light-wave communications, remote sensing, mineral exploration, industrial inspection, *etc.*[2–4] In past decades, dual-band photodetectors, as one group of the most important multispectral photodetectors, have garnered prodigious attention, and a number of dual-band photodetectors including ultraviolet (UV)/UV,[5] UV/visible (VIS),[2,6] VIS/near-infrared (NIR),[7] and infrared (IR)/IR,[8,9] have been realized. Nevertheless, the current dual-band photodetectors are generally fabricated using epitaxial photoactive materials such as semiconductor alloys, type-II superlattices and multiple quantum-wells, which require sophisticated apparatus involving high vacuum and high temperature, and inevitably suffer from shortcomings such as complicated fabrication procedures, lattice and thermal mismatch between epitaxial semiconductor layers, low production yield, high costs and environmental toxicity.[5,10,11] To date, among different dual-band photodetectors, only IR–IR detectors have made successful achievements benefiting from minor lattice mismatch between various epitaxial semiconductor layers and similar epitaxial circumstances.[8,9,12,13] Further development and wide application of dual-band photodetectors have been greatly hampered, and therefore, it is highly desirable to explore facile and cost-effective avenues for designing high-performance dual-band photodetectors.

With the rapid developments in material science, the emergence of many novel functional materials provides new opportunities for designing high-performance photodetectors with exotic functionalities.[14,15] For instance, halide perovskites and related compounds featuring attractive physical properties, *e.g.*, high optical absorption coefficient, high charge carrier mobility, and long carrier lifetime and diffusion length, have shown great potential for exploiting efficient photodetectors.[16–18] Specifically, all inorganic lead-free Cu-based halides, represented by $Cs_3Cu_2I_5$ and $CsCu_2I_3$, have recently revealed appealing

[a] School of Microelectronics, Hefei University of Technology, Hefei, Anhui 230009, P. R. China. E-mail: luolb@hfut.edu.cn
[b] School of Electronics and Information Engineering, Information Materials and Intelligent Sensing Laboratory of Anhui Province, Industry-Education-Research Institute of Advanced Materials and Technology for Integrated Circuits, Anhui University, Hefei, Anhui 230601, P. R. China. E-mail: chaoxie@ahu.edu.cn

† Electronic supplementary information (ESI) available: Fig. S1–S12. See DOI: 10.1039/d1tc04290d

Published on 20 September 2021. Downloaded by HeFei University of Technology on 10/13/2022 3:39:42 AM.

characteristics as building blocks for deep-ultraviolet (DUV) photodetectors and other optoelectronic devices.[19–22] Zhang and co-workers presented the preparation of large-area $Cs_3Cu_2I_5$ crystalline films, which could be applied as highly efficient DUV photodetectors with a responsivity and specific detectivity of 64.9 mA W^{-1} and 6.9×10^{11} Jones, respectively.[23] Shi *et al.* successfully synthesized one-dimensional (1D) $CsCu_2I_3$ nanowires with high crystallinity through anti-solvent engineering.[24] By virtue of the intrinsic anisotropy property, the nanowire-based device could work as a polarized-sensitive UV detector with a photocurrent anisotropy ratio of ∼3.16. In addition, as a class of newly rediscovered 2D materials, group-10 transition metal dichalcogenides (TMDs, *e.g.*, PtS_2, $PtSe_2$, $PtTe_2$, $PdSe_2$, $PdTe_2$) have come under the spotlight as well for their fascinating material properties including high charge carrier mobilities, adjustable narrow bandgaps and outstanding ambient stability.[25–27] These materials have found important applications in various optoelectronics, especially for NIR and IR photodetection.[28–32] Long and colleagues demonstrated a phototransistor made from an exfoliated $PdSe_2$ multilayer, which was highly sensitive to 10.6 μm long-wavelength IR illumination with a responsivity reaching ∼42.1 A W^{-1}.[33] Very recently, Zeng *et al.* reported the van der Waals epitaxial growth of a large-scale $PtTe_2$ multilayer directly on a Si substrate to construct a Schottky junction photodetector, which showed a broadband photodetection capability of up to the middle IR spectral region.[34] Nevertheless, the large-scale synthesis of high-quality 2D $PdTe_2$ and its optoelectronic applications have thus far been scarcely investigated.

In this work, we present a large-scale growth of a 2D $PdTe_2$ multilayer *via* a facile thermal-assisted tellurization approach. By combing a halide $Cs_3Cu_2I_5$, $PdTe_2$ multilayer with Ge, a multiheterostructure-based device was designed, which can successfully function as an electrically adjusted single-band/dual-band photodetector benefiting from the unique optical characteristic and distinct carrier transport behaviour of the multiheterostructure. Remarkably, the device shows a transition from a NIR single-band photodetector with a peak responsivity reaching ∼694.1 mA W^{-1} at 1550 nm at zero bias to a DUV/NIR dual-band photodetector with maximum responsivities attaining ∼744.2 mA W^{-1} and ∼712.5 mA W^{-1} at 265 nm and 1550 nm, respectively, at a small reverse bias. The multiheterostructure-based photodetector also possesses a dual-band optical imaging capability, which can reliably record optical images generated by the DUV and NIR light illuminations.

Results and discussion

Fig. 1a presents a schematic diagram of the designed photodetector, which consists of a $Cs_3Cu_2I_5$, 2D $PdTe_2$ multilayer and Ge substrate to form a multiheterostructure. The device was fabricated by transferring a $PdTe_2$ multilayer atop a Ge substrate with a pre-defined Al_2O_3 open window, followed by spin-coating of a $Cs_3Cu_2I_5$ film, as schematically shown in Fig. S1 (ESI†). In our work, the 2D $PdTe_2$ multilayer was synthesized through a scalable and facile thermal-assisted tellurization approach using a pre-deposited Pd thin film as a precursor *via* the van der Waals epitaxial growth mechanism (Fig. S2, ESI†).[34] The detailed procedures for device fabrication and material synthesis are provided in the Experimental section.

$PdTe_2$ crystallizes into a typical polymeric CdI_2-type structure with a $P\bar{3}m1$ space group.[35] As plotted in Fig. 1b, one Pd atom is covalently bonded with six Te atoms in a repetitive hexagonal unit cell within a single-layer, and the individual single-layer of $PdTe_2$ is bound weakly in the van der Waals style. This material has been confirmed experimentally to be a type-II topological Dirac semimetal, which possesses unique chiral anomaly-related transport and anisotropic magneto-transport features, making it possible for future polarization-sensitive photodetection.[35–38] Fig. 1c and Fig. S3a (ESI†) depict the scanning electron microscopy (SEM) images of the as-synthesized $PdTe_2$ multilayer on a SiO_2/Si substrate. A continuous film with a smooth surface could be clearly observed. The X-ray diffraction (XRD) pattern in Fig. 1d (top panel) shows distinct diffraction peaks at 17.3°, 30.9°, 34.9°, 43.8°, 53.6° and 60.2°, which could be assigned to the (001), (011), (002), (012), (003) and (103) planes of $PdTe_2$, respectively. No extra Pd peaks can be detected in the pattern, signifying that the Pd precursor has been completely transformed into $PdTe_2$ with high phase purity. According to the atomic force microscopy (AFM) image (Fig. 1e), the $PdTe_2$ multilayer was a polycrystalline film consisting of a large number of compact crystalline domains with sizes of about 30-300 nm (Fig. S3b, ESI†). The thickness of the $PdTe_2$ multilayer obtained from the ∼6 nm Pd precursor film was determined to be ∼48.3 nm, and its root mean square roughness was about 5.61 nm. Further transmission electron microscopy (TEM) images at various magnifications in Fig. S3(c–e) (ESI†) show that the $PdTe_2$ multilayer had the unique mosaic-like structure of a 2D layer comprising numerous single-crystalline domains, which was consistent with the result in the AFM image. The high-resolution TEM (HRTEM) image together with the selected-area electron diffraction (SAED) pattern signified a well-defined single-crystalline quality of an individual domain (Fig. 1f). The observed lattice spacing of *ca.* 0.20 nm was ascribed to the (110) plane of $PdTe_2$. Fig. 1g depicts the X-ray photoelectron spectroscopy (XPS) results, where the peaks at about 336.08, 342.08, 586.08 and 576.08 eV were attributed to the orbitals of Pd $3d_{5/2}$, Pd $3d_{3/2}$, Te $3d_{5/2}$ and Te $3d_{3/2}$, respectively. The Raman spectrum of the as-prepared sample was composed of two prominent vibrational modes at ∼74.6 and ∼132.4 cm^{-1}, which corresponded to the in-plane (E_g) and out of-plane (A_{1g}) motions of Te atoms, respectively (Fig. 1h).[39] In addition, the Raman spectra obtained from six random points on a centimeter-sized sample displayed good consistency. Further 2D Raman mapping on the sample over 100×100 μm^2 shows a very narrow distribution of the A_{1g} active mode (Fig. 1i). The results imply a high uniformity and homogeneity of the as-synthesized $PdTe_2$ multilayer. The inset in Fig. 1g shows a photograph of a bared SiO_2/Si substrate (left), a SiO_2/Si substrate covered with ∼6 nm Pd film (middle), and a SiO_2/Si substrate covered with ∼48.3 nm $PdTe_2$ multilayer (right). After successful tellurization, the color of the substrate was changed

 This journal is © The Royal Society of Chemistry 2021

Published on 20 September 2021. Downloaded by HeFei University of Technology on 10/13/2022 3:39:42 AM.

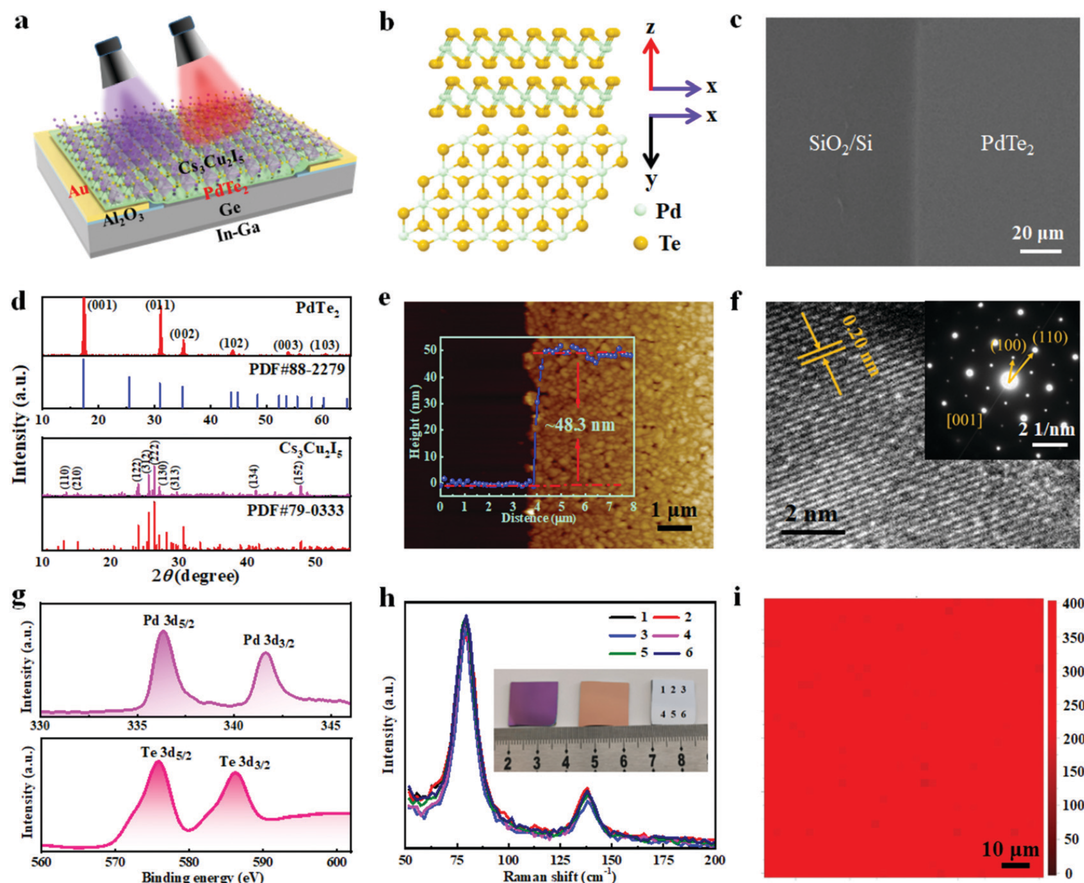

Fig. 1 (a) Schematic diagram of the $Cs_3Cu_2I_5/PdTe_2/Ge$ multiheterostructure-based photodetector. (b) Side (top panel) and top (bottom panel) views of the $PdTe_2$ atomic structure. (c) SEM image of the 2D $PdTe_2$ multilayer on a SiO_2/Si substrate. (d) XRD pattern (top panel) and (e) AFM image of the 2D $PdTe_2$ multilayer synthesized on a SiO_2/Si substrate. Inset in (e) shows the height profile of the $PdTe_2$ multilayer. (d) XRD pattern (bottom panel) of the $Cs_3Cu_2I_5$ film. (f) HRTEM image of the $PdTe_2$ multilayer. Inset in (f) shows the SAED pattern of the sample. (g) XPS spectra of Pd 3d (top panel) and Te 3d (bottom panel). (h) Raman spectrum of six random points on the $PdTe_2$ multilayer. Inset in (g) shows a photograph containing bare SiO_2/Si (left), SiO_2/Si covered with a Pt film (middle), and SiO_2/Si covered with $PdTe_2$ multilayer (right) substrates. (i) 2D Raman mapping of the 2D $PdTe_2$ multilayer over 100×100 μμm^2.

obviously to silvery white with a homogenous surface morphology. The above results confirm that a large-scale homogenous 2D $PdTe_2$ multilayer with excellent quality has been successfully synthesized. Fig. S4a (ESI†) shows the SEM image of the $Cs_3Cu_2I_5$ film, indicating that the film had a relatively high surface coverage with grain sizes of about 400–600 nm. The thickness of the film was ∼570 nm, as determined by the height profile (Fig. S4b, ESI†). A further XRD pattern (Fig. 1d, bottom panel) revealed a series of diffraction peaks at 13.1°, 15.1°, 24.2°, 25.6°, 26.4°, 27.1°, 30.8°, 41.3° and 47.8°, corresponding to the (111), (210), (122), (312), (222), (130), (313), (134) and (152) planes of the orthorhombic $Cs_3Cu_2I_5$, respectively.

We first evaluated the electrical characteristics of the as-constructed $Cs_3Cu_2I_5/PdTe_2/Ge$ multiheterostructure in darkness.

For comparison, the properties of the device before $Cs_3Cu_2I_5$ coating were recorded as well. As depicted in Fig. S5a (ESI†), we note that the $Cs_3Cu_2I_5$ coating had a negligible influence on the electrical properties of the heterostructure. Fig. 2a plots the current *versus* voltage (*I–V*) curve of the multiheterostructure in the dark. Significantly, the multiheterostructure displayed a typical rectifying feature with a forward-to-reverse current ratio of $\sim 4.5 \times 10^2$ at ±1 V, superior to that of many 2D material-based heterostructures in previous reports, *e.g.*, graphene/Ge (∼50),[40] multilayer WS_2/Si (∼200),[41] multilayer $PtSe_2$/Si (∼100)[31] and multilayer $PdSe_2$/Ge (∼5)[42] heterostructures. In view of the good ohmic contacts of $Au/PdTe_2/Au$ and In–Ga/Ge/In–Ga (Fig. S5b, ESI†), as well as the insignificant influence of the $Cs_3Cu_2I_5$ coating layer, the above rectifying behavior should stem exclusively from the heterojunction formed at the $PdTe_2$/Ge interface. In addition, the ideality factor (n) of the heterojunction could be deduced to be ∼1.11 from the ln *I–V* curve (Fig. S5c, ESI†), according to the following formula:[43]

$$n = \frac{q}{K_B T} \frac{\mathrm{d}V}{\mathrm{d}\ln I} \quad (1)$$

where q, K_B and T denote elementary charge, Boltzmann's constant and Kelvin temperature, respectively. The value was in good agreement with the ideal value (n = 1), and was much smaller than that of graphene/GaAs nanocones (n = 3.25)[44] and

Published on 20 September 2021. Downloaded by HeFei University of Technology on 10/13/2022 3:39:42 AM.

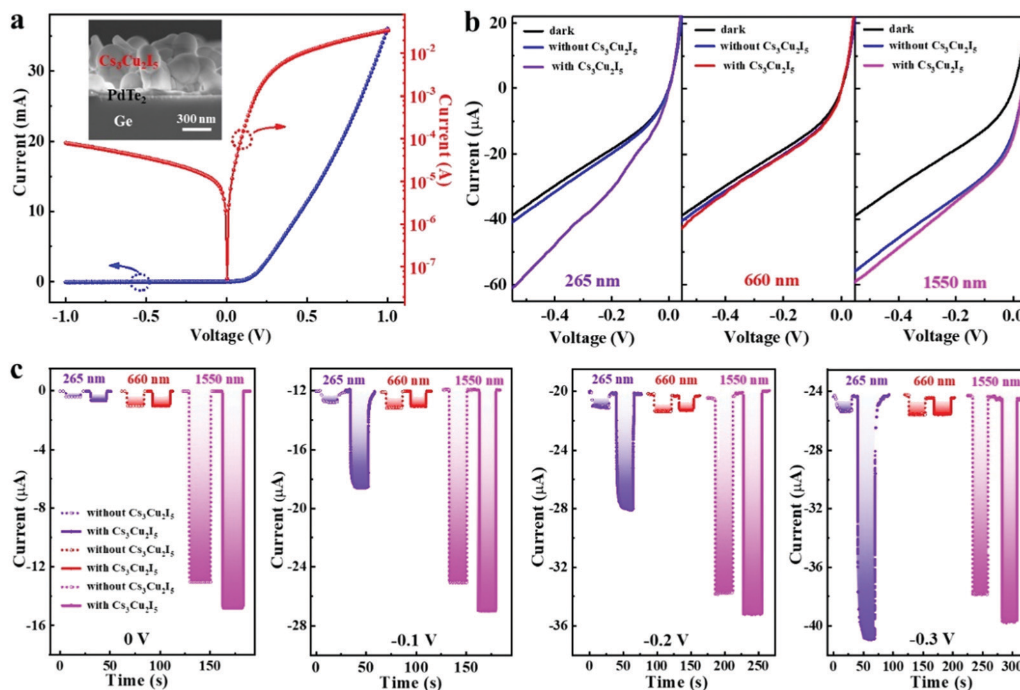

Fig. 2 (a) Dark I–V curves of the multiheterostructure in linear and logarithmic coordinates. The inset shows a cross-sectional SEM image of the multiheterostructure. (b) I–V curves and (c) temporal photoresponse of the $PdTe_2$/Ge heterostructures without and with $Cs_3Cu_2I_5$ coating under light illuminations with wavelengths of 265 nm, 660 nm and 1550 nm, at different bias voltages, respectively.

multilayer MoS_2/Si (n = 1.83)[43] heterojunctions. Furthermore, following the thermionic emission theory, the barrier height (Φ_{BH}) was estimated to be ~708.2 meV (Fig. S5d, ESI†), which was larger than that of graphene/Si (~450 meV)[45] and multilayer MoS_2/Si (~330 meV),[44] and was comparable to that of few-layer $PtSe_2$/Si (~710 meV)[31] heterostructures. The excellent rectifying feature combined with the small ideality factor and large barrier height verified the good quality of the $PdTe_2$/Ge heterojunction.

Next, we examined the optoelectrical properties of the multiheterostructure-based device. Fig. 2b compares the I–V curves of the multiheterostructure, along with those without $Cs_3Cu_2I_5$ coating, under light illuminations with wavelengths of 265 nm (DUV), 660 nm (VIS) and 1550 nm (NIR), respectively, at a constant light intensity of ~1000 μW cm^{-2}. Apparently, without a $Cs_3Cu_2I_5$ coating, the current of the device at reverse bias increased significantly under 1550 nm illumination, while it only showed a slight increase when illuminated with 265 nm and 660 nm irradiations. Interestingly, upon $Cs_3Cu_2I_5$ coating, the current at reverse bias exhibited a dramatic increase at 265 nm, whereas it rose negligibly at 660 nm and somewhat apparently at 1550 nm, when compared with the values without $Cs_3Cu_2I_5$ coating. To deeply understand such an odd photoresponse characteristic, the temporal photoresponse at different bias conditions was measured as well. As plotted in Fig. 2c, with the increase in reverse bias, the photoresponse at 265 nm rose slightly and drastically for the condition without and with $Cs_3Cu_2I_5$ coating, respectively. Specifically, as the bias voltage was changed from 0 V to −0.3 V, the net photocurrent ($I_{ph} = I_{light} - I_{dark}$) at 265 nm increased significantly by more than 26 times from ~0.63 μA to ~16.65 μA with $Cs_3Cu_2I_5$ coating. In addition, in comparison with the value without $Cs_3Cu_2I_5$ coating, the net photocurrent at 265 nm also exhibited ~17-fold increase for the case with $Cs_3Cu_2I_5$ coating at −0.3 V bias voltage. On the contrary, no obvious variation could be found for the net photocurrent at 660 nm neither with the change of bias voltage nor with the coating of $Cs_3Cu_2I_5$. Another intriguing observation is that, compared with the case without $Cs_3Cu_2I_5$ coating, the photoresponse at 1550 nm rose apparently as well after $Cs_3Cu_2I_5$ coating for all bias conditions, while this photoreponse increased only slightly with increasing reverse bias voltage. The above observations implied a reverse bias voltage modulated DUV/NIR single-band/dual-band photodetection characteristic. Fig. 3a summarizes the enhancement of the net photocurrent of the device after $Cs_3Cu_2I_5$ coating at 265 nm and 1550 nm at various bias conditions (I_{ph1} and I_{ph2} denote the net photocurrent without and with $Cs_3Cu_2I_5$ coating, respectively). In comparison with the case without $Cs_3Cu_2I_5$ coating, the photoresponse at 265 nm was drastically enhanced for all bias conditions with the maximum improvement of about 1750% at −0.3 V, whereas the photoresponse at 1550 nm exhibited an improvement of 13.5–14.0% at all bias voltages, upon $Cs_3Cu_2I_5$ coating. As a matter of fact, the improvement in NIR photoresponse was attributed to enhanced photon absorption within Ge due to the anti-reflection of the $Cs_3Cu_2I_5$ film.[46] The inset in Fig. 3a shows the electric field intensity distribution of the $PdTe_2$/Ge heterostructure without and with $Cs_3Cu_2I_5$ coating at 1550 nm.

 This journal is © The Royal Society of Chemistry 2021

Published on 20 September 2021. Downloaded by HeFei University of Technology on 10/13/2022 3:39:42 AM.

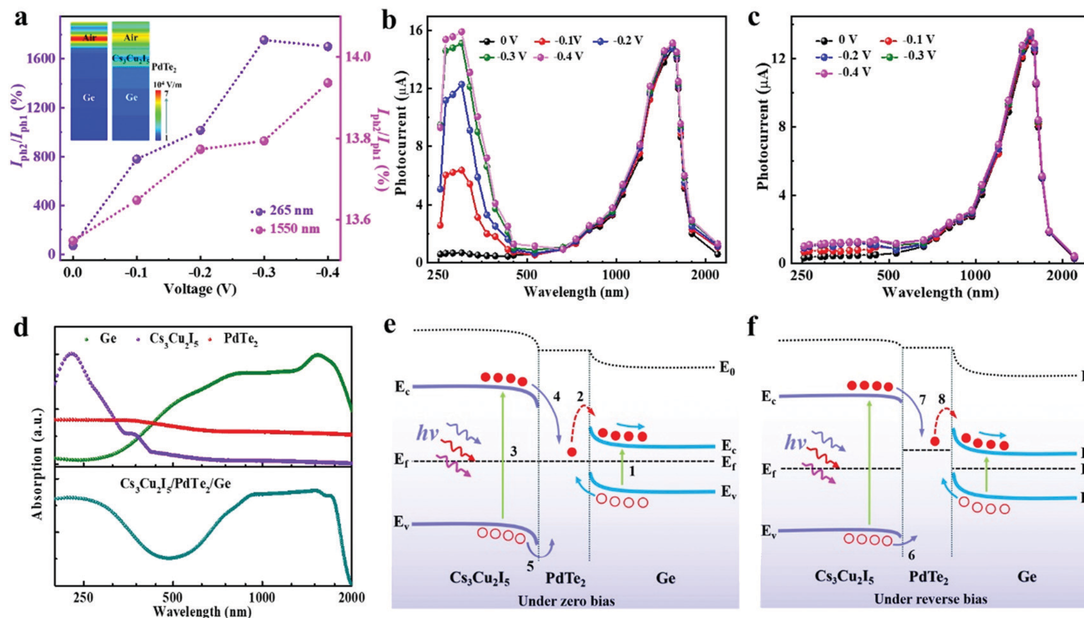

Fig. 3 (a) The enhancement of net photocurrent and electric field distribution (inset) of the $PdTe_2$/Ge heterostructures without and with $Cs_3Cu_2I_5$ coating. The photocurrent as a function of incident light wavelength for the $PdTe_2$/Ge heterostructures (b) with and (c) without $Cs_3Cu_2I_5$ coating, at different bias voltages. (d) Absorption spectra of the $Cs_3Cu_2I_5/PdTe_2$/Ge multiheterostructure, and that of the $Cs_3Cu_2I_5$ film, $PdTe_2$ multilayer, and Ge substrate. Energy band diagram and charge carrier transport of the multiheterostructure under light illumination at (e) zero bias and (f) reverse bias.

With ~570 nm $Cs_3Cu_2I_5$ coating, a stronger electric field intensity could be observed within Ge, indicating a reduced NIR photon absorption loss.

To better illustrate the above intriguing photoresponse properties, we characterized the spectral photoresponse of the multiheterostructure-based device. Fig. 3b and c display the net photocurrent as a function of incident light wavelength from 250–2200 nm (at a fixed intensity of ~1000 μW cm^{-2}), for the device with and without $Cs_3Cu_2I_5$ coating, respectively, at different bias voltages. At zero bias, the photocurrent was very low in the DUV-VIS region (250–730 nm), and started to increase monotonously in the NIR regime (>730 nm) and reached the peak value at ~1550 nm, and then declined gradually with further increasing the light wavelength, for the condition with the $Cs_3Cu_2I_5$ coating (Fig. 3b).

Such an evolution is almost identical with that for the condition without $Cs_3Cu_2I_5$ coating at zero bias (Fig. 3c). Nevertheless, with the increase in reverse bias, the photocurrent at the DUV regime (250–360 nm) showed a dramatic improvement, rendering dual photoresponse peaks located at ~260–300 nm and ~1450–1600 nm, respectively, for the condition with $Cs_3Cu_2I_5$ coating (Fig. 3b). This circumstance was in sharp contrast to that of the device without $Cs_3Cu_2I_5$ coating, in which increasing reverse bias only led to a slight enhancement in photocurrent in the DUV region (Fig. 3c). These results again confirmed the electrically modulated DUV/NIR single-band/dual-band detection capability of the $Cs_3Cu_2I_5/PdTe_2$/Ge multiheterostructure-based photodetector.

The above electrically adjusted DUV/NIR single-band/dual-band photosensing nature could be correlated with the unique optical property of the $Cs_3Cu_2I_5/PdTe_2$/Ge multiheterostructure and its distinctive carrier transport behavior. Fig. 3d plots the absorption spectrum of the $Cs_3Cu_2I_5/PdTe_2$/Ge multiheterostructure, along with that of the $Cs_3Cu_2I_5$ film, $PdTe_2$ multilayer and Ge substrate for comparison. Clearly, the combination of the three components led to a dual-band optical absorption characteristic with strong optical absorption in the DUV and NIR regimes. Furthermore, the carrier transport behavior could be understood by analyzing the energy band diagram of the multiheterostructure. The ~48.3 nm-thick 2D $PdTe_2$ multilayer displayed semi-metallic characteristics and its work function (W_f) was determined to be ~4.80 eV according to the ultraviolet photoemission spectrum (UPS) (Fig. S6, ESI†).[35] The $Cs_3Cu_2I_5$ film with p-type electrical properties has the conduction band minimum (E_c), Fermi level (E_f) and vacuum band maximum (E_v) of −3.02 eV, −5.36 eV and −6.88 eV, respectively,[47] and the n-Ge with a resistivity of 0.1–6 Ω cm held the E_c, E_f, and E_v values of −4.13 eV, −4.37 eV and −4.81 eV, respectively, in roughness.[48] Therefore, because of the difference in their E_f values (Fig. S7a, ESI†), electrons would diffuse from Ge towards $Cs_3Cu_2I_5$ to attain thermal equilibrium, when the three components are in contact with each other. Such an electron diffusion process caused the energy levels near the lower/upper surface of $Cs_3Cu_2I_5$/Ge to bend downward/upward, rendering the production of an internal electric field at the multiheterostructure interface with a direction from Ge to $Cs_3Cu_2I_5$. Under zero bias, as depicted in Fig. 3e, when illuminated with VIS-NIR light, charge carrier generation induced by photon absorption took place primarily within the Ge (process 1) considering the relatively high transparency of the 2D $PdTe_2$ multilayer (Fig. S7b, ESI†), and the photocarriers were rapidly separated by the internal electric field. Subsequently, the electrons

Published on 20 September 2021. Downloaded by HeFei University of Technology on 10/13/2022 3:39:42 AM.

crossing the Ge substrate were collected by the bottom In–Ga electrode, while the holes transporting through the $PdTe_2$ arrived at the Au electrode, resulting in the generation of photocurrent. In addition, following the thermal photoemission process, electrons generated in $PdTe_2$ holding energy exceeding the barrier height of the heterostructure could also contribute to the photocurrent (process 2). Of note, incident light with a short wavelength was absorbed near the upper surface of the Ge (Fig. S8, ESI†), where a severe carrier recombination to lower photoresponse existed due to the presence of surface defects and/or dangling bonds.[49] This explained the weak photoresponse at the VIS region, and also the similar phenomenon observed at the DUV-VIS regime in the case without $Cs_3Cu_2I_5$ coating (Fig. 3c). When under DUV illumination, $Cs_3Cu_2I_5$ could absorb the incident light to produce photocarriers (process 3). Although photoexcited electrons were easily injected into $PdTe_2$ (process 4), photoexcited holes could hardly be diffused to $PdTe_2$ due to the large energy barrier (process 5). Thus, the majority of photocarriers would be recombined within $Cs_3Cu_2I_5$, giving a poor photoresponse at the DUV region. Therefore, the device could only exhibit an NIR single-band photodetecting ability at zero bias. On the contrary, under reverse bias, the band bending at the $Cs_3Cu_2I_5$ side was greatly reduced, which lowered the energy barrier for holes to diffuse towards $PdTe_2$ (Fig. 3f). Thus, upon DUV illumination, a large number of photoexcited holes in $Cs_3Cu_2I_5$ could readily diffuse to $PdTe_2$ (process 6), and be collected by the Au electrode. Meanwhile, thanks to the large energy level difference between E_c of $Cs_3Cu_2I_5$ and E_f of $PdTe_2$, photoexcited electrons injected from $Cs_3Cu_2I_5$ to $PdTe_2$ (process 7) possessed enough energy to surmount the barrier height and be swept into the E_c of Ge (process 8), and ultimately be collected by the In–Ga electrode. The above processes gave a sizeable photoresponse at the DUV regime. Therefore, a DUV and NIR dual-band photosensing behavior could be observed under reverse bias.

Next, we studied the photoresponse of the multiheterostructure-based device under 265 nm and 1550 nm illuminations with different light intensities. Fig. 4a and b depict the *I–V* curves of the device in darkness and under 265 nm (0.068–1.005 mW cm^{-2}) and 1550 nm (0.080–1.815 mW cm^{-2}) irradiations, respectively. Remarkably, the current at reverse bias rose monotonously with increasing light intensity for both light wavelengths, which could be ascribed to an increased number of photogenerated carriers under light excitation with a higher intensity.[30] However, careful analysis found that the device exhibited different photoresponse behaviors at two wavelengths. Fig. S9a and b (ESI†) show the enlarged *I–V* curves in darkness and under 265 nm and 1550 nm illuminations, respectively. One can see clearly that the device displayed a pronounced photovoltaic effect at 1550 nm, *i.e.*, sizeable photocurrents at zero bias and photovoltages, while this behavior was very weak at 265 nm. Such a phenomenon was in good agreement with the above energy band analysis, where the DUV illumination could only excite a considerable photoresponse at reverse bias while the NIR irradiation could induce impressive photoresponse at zero bias. Note that the strong photovoltaic effect enabled our device to function as a self-driven NIR photodetector without an external power supply. Fig. 4c and d plot the relationships between photocurrent at different biases (or photovoltage) and light intensity for both wavelengths, revealing that photovoltage and photocurrents increased gradually with increasing light intensity for all conditions. The dependence of photocurrent on

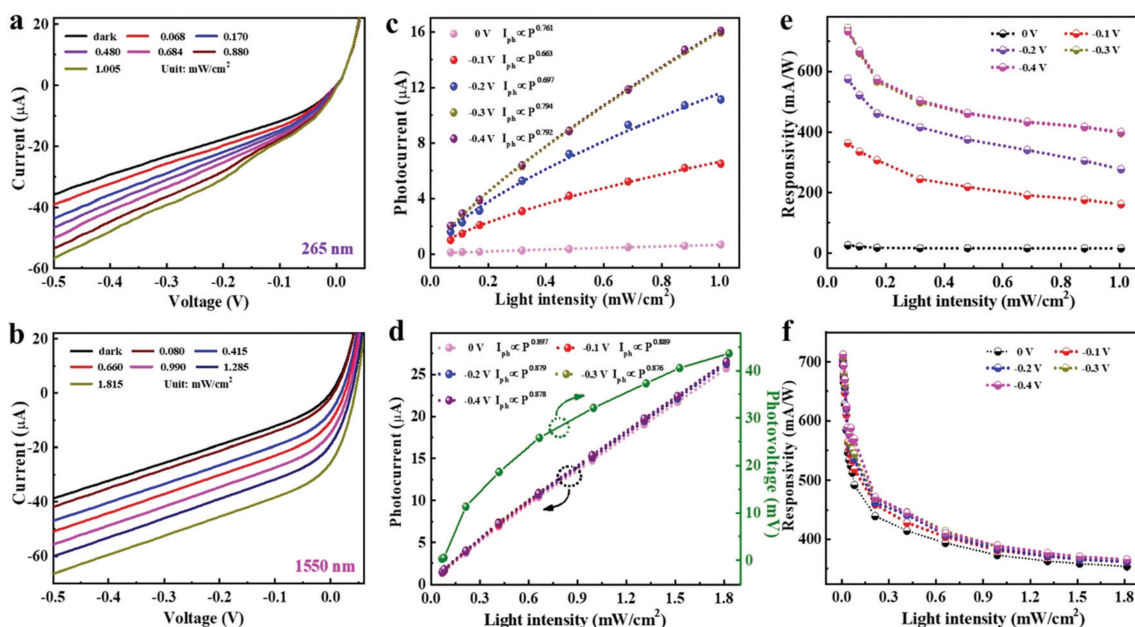

Fig. 4 *I–V* curves of the multiheterostructure-based photodetector under (a) 265 nm and (b) 1550 nm light illumination with different light intensities. Photocurrent (photovoltage) *versus* light intensity under (c) 265 nm and (d) 1550 nm light illuminations at different bias voltages. Responsivity *versus* light intensity under (e) 265 nm and (f) 1550 nm light illuminations at different bias voltages.

This journal is © The Royal Society of Chemistry 2021

Published on 20 September 2021. Downloaded by HeFei University of Technology on 10/13/2022 3:39:42 AM.

light intensity could be described by using a commonly employed power law: $I_{ph} = P_{\lambda}^{\theta}$, where P_{λ} represents the light intensity. As shown in Fig. 4c and d, the value of θ was deduced to be 0.66–0.80 for 265 nm and around 0.88 for 1550 nm at different bias voltages, respectively. The non-ideal θ values of less than 1 implied the existence of recombination loss due to complicated carrier recombination processes.[43,50] The temporal photoresponse was also explored under both illuminations with different light intensities, as shown in Fig. S9c and d (ESI†). Clearly, the device displayed good photo-switch characteristics for all illumination conditions, and the photoresponse had the same evolution tendency with increasing light intensity as observed in the *I–V* curves. The I_{light}/I_{dark} ratio could reach as high as 4.3×10^3 under a 1550 nm incident light with a higher intensity of 15.17 mW cm^{-2} (Fig. S9e, ESI†).

To quantitatively evaluate the device performance, the responsivity (*R*) was then calculated according to the following equation:[51]

$$R = \frac{I_{ph}}{SP} = \frac{e\lambda}{hc}\mathrm{EQE} \quad (2)$$

where S, e, λ, h and c are the effective device area (S = 0.04 cm^2), the elementary charge, the wavelength of incident light, Planck's constant and the speed of incident light, respectively. Accordingly, the R was 25.7 mA W^{-1} at zero bias and increased remarkably to as high as 362.9, 575.8, 744.2, and 732.5 mA W^{-1} at −0.1, −0.2, −0.3, and −0.4 V at 265 nm at ∼68 μW cm^{-2} light intensity, and it was 694.1 mA W^{-1} at zero bias and increased slightly to 698.4, 703.1, 707.2, and 712.5 mA W^{-1} at −0.1, −0.2, −0.3, and −0.4 V at 1550 nm at ∼80 μW cm^{-2} light intensity. Of note, the R at 265 nm was superior to commercial UV-enhanced Si photodiodes (typically 100–150 mA W^{-1}, OSI optoelectronics series products) and a graphene-enhanced Si Schottky photodiode (∼140 mA W^{-1} in 200–400 nm),[52] while the value at 1550 nm was significantly higher than that of an NIR photodetector composed of graphene/Ge (51.8–185 mA W^{-1}),[40,53] and was comparable to other group-10 TMD/Ge (530–691 mA W^{-1}),[42,54,55] as well as commercial Ge NIR photodiodes (850–950 mA W^{-1}, Thorlabs series products). Fig. 4e and f describe the dependence of R values on light intensity for 265 nm and 1550 nm illuminations, respectively. It was found that the R declined gradually with the increase in light intensity for all bias conditions, which could be attributed to the intensified carrier recombination activity at a relatively larger light intensity.[43] Additionally, the EQE value was below 15% at the DUV region at zero bias, which could be enhanced dramatically to as high as about 340% at a reverse bias of −0.4 V (Fig. S10, ESI†).

In addition, we examined specific detectivity (D^*) and noise equivalent power (NEP), which determined the detection limit of a photodetector. The two parameters are normally described as follows:[51]

$$D^* = \frac{(Sf)^{1/2}}{\mathrm{NEP}} \quad (3)$$

$$\mathrm{NEP} = \frac{\overline{i_n^2}^{1/2}}{R} \quad (4)$$

where f is the bandwidth, and $\overline{i_n^2}^{1/2}$ is the root-mean-square value of the noise current, respectively. The value of $\overline{i_n^2}^{1/2}$ at f = 1 Hz was extracted to be 1.01×10^{-12}, 4.2×10^{-10}, 4.3×10^{-10}, and 7.8×10^{-10} A Hz$^{-1/2}$ at a bias of 0, −0.1, −0.2, and −0.3 V for the present device (Fig. S11, ESI†). Accordingly, the NEP was deduced to be 3.93×10^{-11}, 1.16×10^{-9}, 1.09×10^{-9}, and 1.05×10^{-9} WHz$^{-1/2}$ at 265 nm, and 1.46×10^{-12}, 6.01×10^{-10}, 8.96×10^{-10}, and 1.10×10^{-9} WHz$^{-1/2}$ at 1550 nm, respectively, at these bias voltages. Therefore, the D^* was 5.08×10^9, 1.73×10^8, 1.83×10^8, and 1.91×10^8 Jones at 265 nm, and 1.37×10^{11}, 3.33×10^8, 2.23×10^8, 1.81×10^8 Jones at 1550 nm, respectively, at the above bias voltages. Although the D^* at 265 nm was somewhat lower than that of previously reported DUV photodetectors,[23,24] the value at 1550 nm was comparable to 2D material/Ge heterojunction NIR photodetectors in previous reports.[40,42,53,54] Higher D^* could be expected through raising the heterojunction barrier height to reduce the device noise by means of interface passivation techniques.[56]

We also studied the response speed of our photodetector, which was a critical device parameter reflecting the capability of a photodetector to detect fast varied photonic signals. Fig. 5a shows an individual temporal photoresponse curve at 265 nm, revealing a rise/fall time of 3.8/3.1 s.[42] In addition, Fig. 5b presents the temporal photoresponse at 1550 nm with varied modulation frequencies from 0.5 kHz to 10 kHz, showing that the device had a stable, repeatable, and reversible photoresponse for all frequencies. The dependence of the relative balance $(V_{max} - V_{min})/V_{max}$ on the light frequency was described in Fig. 5c, giving a −3 dB frequency (f_{-3dB}: defined as the frequency where the photoresponse declined to 70.7% of its maximum value) of ∼10 kHz at 1550 nm. From a magnified photoresponse curve, the rise/fall time was deduced to be 24.9/26.2 μs (Fig. 5d), which was comparable to and even faster than many 2D material-based heterojunction photodetectors.[15,30,43,51,55] The fast response speed at 1550 nm was related to the fast separation and transportation of photocarriers by the strong internal electric field at the $PdTe_2$/Ge interface. Additionally, the difference in response speed for both wavelengths could be ascribed to the distinct photocurrent generation processes under DUV and NIR illuminations. First, the photocarriers needed to be transported across grain boundaries within the polycrystalline $Cs_3Cu_2I_5$ (inset in Fig. 2a). Second, as discussed in the above energy band diagrams, the photoexcited electrons in $Cs_3Cu_2I_5$ had to move firstly to $PdTe_2$ and were then injected into Ge. The two reasons retarded the quick carrier transport and were responsible for the relatively slow response speed at the DUV regime. Of note, the response speed at 265 nm was still comparable to many ultrawide bandgap semiconductor-based DUV photodetectors.[57]

The advantage of our photodetector also lay in its excellent air stability and repeatability. Fig. S12a and b (ESI†) exhibit the temporal photoresponse before and after storage in ambient conditions without any protection for 30 days, at 265 nm and

Published on 20 September 2021. Downloaded by HeFei University of Technology on 10/13/2022 3:39:42 AM.

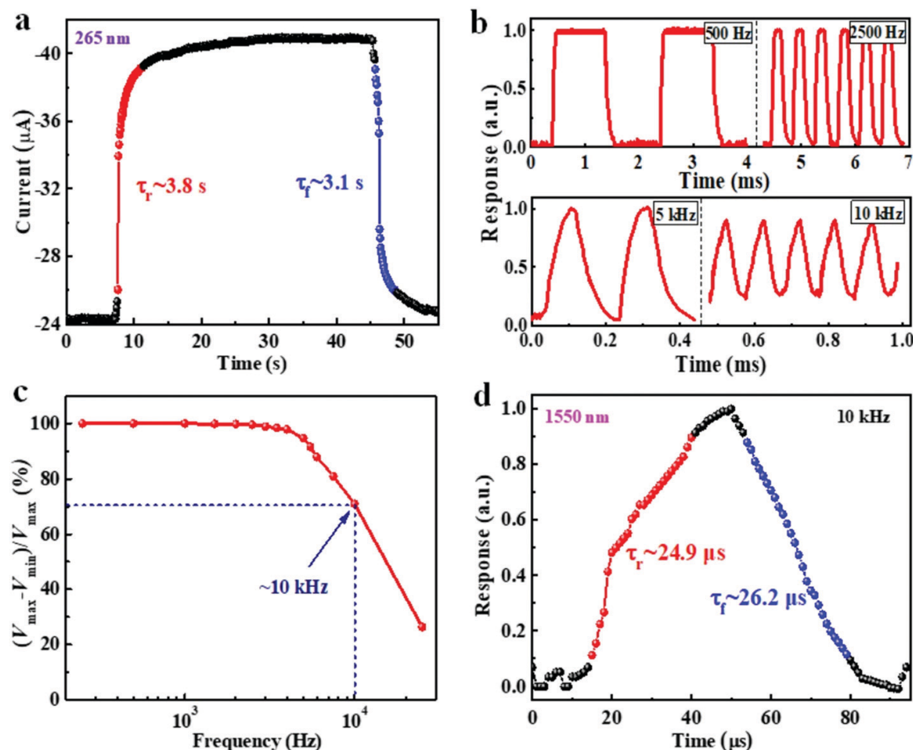

Fig. 5 (a) A single cycle of temporal photoresponse of the multiheterostructure-based photodetector at 265 nm. (b) Temporal photoresponse under 1550 nm light illuminations with different modulating frequencies. (c) Relative balance $(V_{max} - V_{min})/V_{max}$ *versus* frequency of the incident light, giving a −3 dB cutoff frequency of ∼10 kHz. (d) A single cycle of temporal photoresponse at 1550 nm.

1550 nm, respectively. Clearly, the photoresponse characteristics were well-preserved with good cycling stability. In addition, as observed in Fig. S12c (ESI†), the device could also retain its initial response properties with negligible degradation after over 500 hundred operations. This good air stability and repeatability could be ascribed to the following two aspects: (i) as confirmed by the XRD pattern and Raman spectra (Fig. S12d and e, ESI†), the all-inorganic $Cs_3Cu_2I_5$ film and the 2D $PdTe_2$ multilayer had a high ambient stability. (ii) The $Cs_3Cu_2I_5$ and $PdTe_2$ could effectively prevent oxidation at the heterojunction interface in this well-designed vertically stacked device geometry.

Finally, the ability of the present photodetector to serve as an optical image sensor was investigated. Fig. 6a displays the setup for imaging measurements, where a lab-made shadow mask controlled by a stepper motor was placed between the light source and the photodetector, and only the illumination penetrating the hollow pattern could shine upon the photodetector. With the progressive movement of the shadow mask along the horizontal (*x*-) or vertical (*y*-) direction, the position-resolved current of the device was recorded by a SourceMeter. After measurement of all pixels, the current values were incorporated into a 2D current map. In total, three light illuminations, namely, 265 nm DUV illumination, 660 nm VIS illumination, and 1550 nm NIR illumination, were employed as the light sources. Fig. 6b compares the 2D current maps at these wavelengths. Evidently, the images of ''DUV'' (at 265 nm) and ''NIR'' (at 1550 nm) could be clearly distinguished with a decent spatial resolution, whereas the image of ''VIS'' (at 660 nm) had to be identified, implying the DUV/NIR dual-band imaging capability of our photodetector.

Experimental section

Materials preparation and characterization

The large-scale 2D $PdTe_2$ multilayer was synthesized *via* a thermal-assisted tellurization technique. Briefly, a Pd metal film with a thickness of ∼6 nm was firstly deposited onto a SiO_2/Si substrate through electron beam evaporation. Then, the substrate was transferred to the central zone of a tube furnace and high-purity Te powder (99.99% in purity) was placed at the upstream side about ∼10 cm away from the substrate. The temperature of the central zone was set to 300 °C, while the temperature of the zone where the Te source was placed would reach ∼200 °C. 100 sccm Ar gas was used to transport the evaporated Te to the substrate to participate in tellurization. After about 60 min, the tube furnace was naturally cooled down to ambient temperature, and the 2D $PdTe_2$ multilayer with a silvery white appearance was acquired on the substrate. The $Cs_3Cu_2I_5$ film was prepared *via* a simple spin-coating method. 545.58 mg CsI (purity) and 266.63 mg CuI (purity) were added sequentially into a mixed solvent of 200 μL of dimethylsulfoxide (DMSO, >99.9%) and 800 μL of *N*,*N*-dimethylformamide

 This journal is © The Royal Society of Chemistry 2021

Published on 20 September 2021. Downloaded by HeFei University of Technology on 10/13/2022 3:39:42 AM.

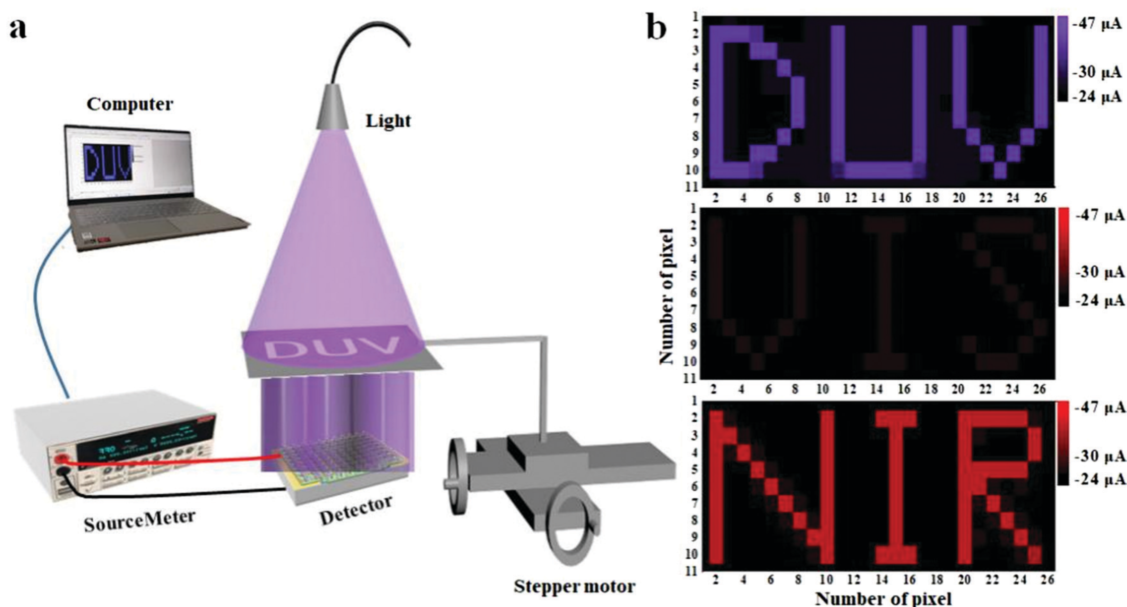

Fig. 6 (a) Schematic diagram of the setup for imaging measurements. (b) 2D current maps under 265 nm, 660 nm, and 1550 nm illuminations at a bias of −0.3 V, showing DUV/NIR dual-band imaging capability.

(DMF, 99.8%), and stirred at 25 °C for 60 min to prepare the precursor solution of $Cs_3Cu_2I_5$. 50 μL of the precursor solution was spin-coated onto a substrate at 1500 rpm for 10 s and 3000 rpm for another 30 s. After sequential annealing at 80 °C for 5 min and 100 °C for another 20 min, the $Cs_3Cu_2I_5$ film was obtained on the substrate.

The morphology of the $PdTe_2$ multilayer and $Cs_3Cu_2I_5$ film was observed by using SEM (Hitachi, SU8020). The topography and height profile were studied by AFM (Benyuan Nanotech Com, CSPM-4000). The crystal structure was examined by TEM (JEOL Model JEM-2100F). The XRD pattern was recorded on an X-ray diffractometer (Rigaku D/max-rB). The absorption spectra were measured by using a Shimadzu UV-2550 UV-vis spectrophotometer. An HR Evolution Raman spectrometer (Horiba Jobin Yvon) equipped with a 488 nm argon-ion laser was used to record the Raman spectra. XPS and UPS measurements were performed on an Escalab 250Xi (Thermo Scientific) spectrometer using a monochromatic Al Kα source (1486.6 eV) and Mg KR line, respectively. The refractive index (n') and extinction coefficient (k) of the $Cs_3Cu_2I_5$ film and $PdTe_2$ multilayer were measured by an ellipsometer (J. A. Woollam, RC2 UI).

Device fabrication and analysis

To fabricate the $Cs_3Cu_2I_5$/$PdTe_2$/Ge multiheterostructure-based photodetector, an open window (0.2 × 0.2 cm^2) was firstly defined on an n-Ge substrate (resistivity: 0.1–6 Ω cm^{-1}) covered with an ~80 nm atomic layer deposition-grown Al_2O_3 insulating layer by traditional photolithography, followed by removing the insulating layer within the window region with a wet etching process. Then, a 50 nm-thick Au top electrode was deposited on the Al_2O_3 layer using a lab-build shadow mask through high-vacuum electron beam evaporation. The as-synthesized $PdTe_2$ multilayer was directly transferred atop the substrate *via* a polymethyl methacrylate (PMMA)-assisted transfer technique. After that, a $Cs_3Cu_2I_5$ film was prepared atop the $PdTe_2$ multilayer by a spin-coating technique. Finally, an indium–gallium (In–Ga) alloy was attached to the rear side of the Ge substrate to serve as the bottom electrode.

A Keithley 4200-SCS semiconductor analyser was used to perform electrical measurement of the photodetector. For the photoresponse study, light emitting diodes (LEDs, Thorlabs products) with various wavelengths were employed as the light sources. To record the response time, a signal generator (Tektronix, TDS2022B) was employed to power the LED to produce pulsed light irradiation with different frequencies, and the output signal was monitor by an oscilloscope (Tektronix, TDS2012B). Prior to use, a power meter (Thorlabs GmbH., PM 100D) was employed to calibrate the light intensity of all light sources. All measurements were performed under ambient conditions at room temperature.

Theoretical simulation

Synopsys Sentaurus TCAD was employed to simulate the photon absorption rate of the n-Ge substrate (Sb doped, carrier concentration: 10^{15} cm^{-3}) in a 2D structure with dimensions of 20 μm × 180 μm and 20 μm × 10 μm, respectively. A beam of incident light with different wavelengths was introduced to the front side of the Ge surface at an incident angle of 90°. COMSOL was used to simulate the electric field distribution of the $PdTe_2$/Ge heterostructures with and without $Cs_3Cu_2I_5$ coating at 1550 nm. The thicknesses of $Cs_3Cu_2I_5$, $PdTe_2$ and Ge were set to be 570 nm, 48 nm and 200 μm, respectively. The designed structure was covered by a semi-infinite air layer with a permittivity of 1. The optical constants of the $Cs_3Cu_2I_5$ film and $PdTe_2$ multilayer were n' = 1.05863, k = 0.03856 and n' = 3.10697, k = 6.44695, respectively, at 1550 nm. The optical

Published on 20 September 2021. Downloaded by HeFei University of Technology on 10/13/2022 3:39:42 AM.

constants of Ge were obtained from the data library of the software.

Conclusions

In summary, large-scale synthesis of a high-quality 2D $PdTe_2$ multilayer has been demonstrated. By rationally designing a multiheterostructure containing a halide $Cs_3Cu_2I_5$ film on a 2D $PdTe_2$/Ge heterojunction, electrically adjusted DUV/NIR single-band/dual-band photodetection has been successfully realized. At zero bias, the device exhibited an NIR single-band photodetection feature with peak responsivity attaining $\sim$694.1 mA W^{-1} at 1550 nm, while, at a small reverse bias, it could show a DUV/NIR dual-band photodetection capability with maximum responsivities reaching $\sim$744.2 mA W^{-1} and $\sim$712.5 mA W^{-1} at 265 nm and 1550 nm, respectively. It was also demonstrated that the present device possessed DUV/NIR dual-band optical image sensing ability with a decent spatial resolution. Given the unique electrically modulated DUV/NIR single-band/dual-band photodetection characteristic and high ambient stability, the $Cs_3Cu_2I_5$/$PdTe_2$/Ge multiheterostructure-based photodetector will hold great promise for high-performance multifunctional photodetection towards applications in complex environments.

Author contributions

C. X. and L. L. conceived the experiments. C. X. and Y. L. synthesized the materials, and fabricated and characterized the devices. Y. L. conducted the simulations. C. D., X. T., W. Y., and C. W. assisted with the work on material growth, characterization and result analysis. C. X., and L. L. supervised the project. All authors discussed the results and co-wrote the manuscript.

Conflicts of interest

The authors declare they have no competing interests.

Acknowledgements

This work was financially supported by the National Natural Science Foundation of China (NSFC, No. 51902078, 62074048, 61675062), the Anhui Provincial Natural Science Foundation (2008085MF205), and the Fundamental Research Funds for the Central Universities (JZ2020HGTB0051, PA2020GDKC0014, JZ2018HGPB0275). The authors acknowledge Mr Huirong Su from Genuine Optronics Ltd. for providing the optical constant measurements and corresponding data analysis.

Notes and references

1 X. Tang, M. M. Ackerman, M. Chen and P. Guyot-Sionnest, *Nat. Photonics*, 2019, **13**, 277–282.
2 M. Dai, H. Chen, R. Feng, W. Feng, Y. Hu, H. Yang, G. Liu, X. Chen, J. Zhang, C.-Y. Xu and P. Hu, *ACS Nano*, 2018, **12**, 8739–8747.
3 L. Li, H. Chen, Z. Fang, X. Meng, C. Zuo, M. Lv, Y. Tian, Y. Fang, Z. Xiao, C. Shan, Z. Xiao, Z. Jin, G. Shen, L. Shen and L. Ding, *Adv. Mater.*, 2020, **32**, 1907257.
4 N. Gautam, M. Naydenkov, S. Myers, A. V. Barve, E. Plis, T. Rotter, L. R. Dawson and S. Krishna, *Appl. Phys. Lett.*, 2011, **98**, 121106.
5 L. Su, H. Chen, X. Xu and X. Fang, *Laser Photonics Rev.*, 2017, **11**, 1700222.
6 Y. Zhang, W. Xu, X. Xu, J. Cai, W. Yang and X. Fang, *J. Phys. Chem. Lett.*, 2019, **10**, 836–841.
7 K. Swaminathan, T. J. Grassman, L.-M. Yang, Q. Gu, M. J. Mills and S. A. Ringel, *J. Appl. Phys.*, 2011, **110**, 063109.
8 J. Huang, W. Ma, Y. Zhang, Y. Cao, W. Huang and C. Zhao, *IEEE Electron Device Lett.*, 2017, **38**, 1266–1269.
9 T. D. Nguyen, J. O. Kim, Y. H. Kim, E. T. Kim, Q. L. Nguyen and S. J. Lee, *AIP Adv.*, 2018, **8**, 025015.
10 A. Haddadi, A. Dehzangi, R. Chevallier, S. Adhikary and M. Razeghi, *Sci. Rep.*, 2017, **7**, 3379.
11 G. Sarusi, *Infrared Phys. Technol.*, 2003, **44**, 439–444.
12 E. Plis, S. Myers, D. Ramirez, E. P. Smith, D. Rhiger, C. Chen, J. D. Phillips and S. Krishna, *Infrared Phys. Technol.*, 2015, **70**, 93–98.
13 A. Khoshakhlagh, J. B. Rodriguez, E. Plis, G. D. Bishop, Y. D. Sharma, H. S. Kim, L. R. Dawson and S. Krishna, *Appl. Phys. Lett.*, 2007, **91**, 263504.
14 H. Wang and D. H. Kim, *Chem. Soc. Rev.*, 2017, **46**, 5204–5236.
15 M. Buscema, J. O. Island, D. J. Groenendijk, S. I. Blanter, G. A. Steele, H. S. J. van der Zant and A. Castellanos-Gomez, *Chem. Soc. Rev.*, 2015, **44**, 3691–3718.
16 M. Ahmadi, T. Wu and B. Hu, *Adv. Mater.*, 2017, **29**, 1605242.
17 W. Tian, H. Zhou and L. Li, *Small*, 2017, **13**, 1702107.
18 C. Xie, C. Liu, H. Loi and F. Yan, *Adv. Funct. Mater.*, 2020, **30**, 1903907.
19 Y. Li, Z. Shi, W. Liang, L. Wang, S. Li, F. Zhang, Z. Ma, Y. Wang, Y. Tian, D. Wu, X. Li, Y. Zhang, C. Shan and X. Fang, *Mater. Horiz.*, 2020, **7**, 530–540.
20 T. Jun, K. Sim, S. Iimura, M. Sasase, H. Kamioka, J. Kim and H. Hosono, *Adv. Mater.*, 2018, **30**, 1804547.
21 M. Zhang, J. Zhu, B. Yang, G. Niu, H. Wu, X. Zhao, L. Yin, T. Jin, X. Liang and J. Tang, *Nano Lett.*, 2021, **21**, 1392–1399.
22 Z. Li, Z. Li, Z. Shi and X. Fang, *Adv. Funct. Mater.*, 2020, **30**, 2002634.
23 Z.-X. Zhang, C. Li, Y. Lu, X.-W. Tong, F.-X. Liang, X.-Y. Zhao, D. Wu, C. Xie and L.-B. Luo, *J. Phys. Chem. Lett.*, 2019, **10**, 5343–5350.
24 Y. Li, Z. Shi, L. Wang, Y. Chen, W. Liang, D. Wu, X. Li, Y. Zhang, C. Shan and X. Fang, *Mater. Horiz.*, 2020, **7**, 1613–1622.
25 L. Pi, L. Li, K. Liu, Q. Zhang, H. Li and T. Zhai, *Adv. Funct. Mater.*, 2019, **29**, 1904932.
26 Y. Zhao, J. Qiao, P. Yu, Z. Hu, Z. Lin, S. P. Lau, Z. Liu, W. Ji and Y. Chai, *Adv. Mater.*, 2016, **28**, 2399–2407.

This journal is © The Royal Society of Chemistry 2021

Published on 20 September 2021. Downloaded by HeFei University of Technology on 10/13/2022 3:39:42 AM.

27 W. L. Chow, P. Yu, F. Liu, J. Hong, X. Wang, Q. Zeng, C.-H. Hsu, C. Zhu, J. Zhou, X. Wang, J. Xia, J. Yan, Y. Chen, D. Wu, T. Yu, Z. Shen, H. Lin, C. Jin, B. K. Tay and Z. Liu, *Adv. Mater.*, 2017, **29**, 1602969.
28 Y. Zhao, J. Qiao, Z. Yu, P. Yu, K. Xu, S. P. Lau, W. Zhou, Z. Liu, X. Wang, W. Ji and Y. Chai, *Adv. Mater.*, 2017, **29**, 1604230.
29 X. Yu, P. Yu, D. Wu, B. Singh, Q. Zeng, H. Lin, W. Zhou, J. Lin, K. Suenaga, Z. Liu and Q. J. Wang, *Nat. Commun.*, 2018, **9**, 1545.
30 L.-H. Zeng, D. Wu, S.-H. Lin, C. Xie, H.-Y. Yuan, W. Lu, S. P. Lau, Y. Chai, L.-B. Luo, Z.-J. Li and Y. H. Tsang, *Adv. Funct. Mater.*, 2019, **29**, 1806878.
31 C. Yim, N. McEvoy, S. Riazimehr, D. S. Schneider, F. Gity, S. Monaghan, P. K. Hurley, M. C. Lemme and G. S. Duesberg, *Nano Lett.*, 2018, **18**, 1794–1800.
32 J. Yuan, T. Sun, Z. Hu, W. Yu, W. Ma, K. Zhang, B. Sun, S. P. Lau, Q. Bao, S. Lin and S. Li, *ACS Appl. Mater. Interfaces*, 2018, **10**, 40614–40622.
33 M. Long, Y. Wang, P. Wang, X. Zhou, H. Xia, C. Luo, S. Huang, G. Zhang, H. Yan, Z. Fan, X. Wu, X. Chen, W. Lu and W. Hu, *ACS Nano*, 2019, **13**, 2511–2519.
34 L. Zeng, D. Wu, J. Jie, X. Ren, X. Hu, S. P. Lau, Y. Chai and Y. H. Tsang, *Adv. Mater.*, 2020, **32**, 2004412.
35 C. Guo, Y. Hu, G. Chen, D. Wei, L. Zhang, Z. Chen, W. Guo, H. Xu, C.-N. Kuo, C. S. Lue, X. Bo, X. Wan, L. Wang, A. Politano, X. Chen and W. Lu, *Sci. Adv.*, 2020, **6**, eabb6500.
36 H.-J. Noh, J. Jeong, E.-J. Cho, K. Kim, B. I. Min and B.-G. Park, *Phys. Rev. Lett.*, 2017, **119**, 016401.
37 W. Zheng, R. Schönemann, N. Aryal, Q. Zhou, D. Rhodes, Y.-C. Chiu, K.-W. Chen, E. Kampert, T. Förster, T. J. Martin, G. T. McCandless, J. Y. Chan, E. Manousakis and L. Balicas, *Phys. Rev. B*, 2018, **97**, 235154.
38 F. Fei, X. Bo, R. Wang, B. Wu, J. Jiang, D. Fu, M. Gao, H. Zheng, Y. Chen, X. Wang, H. Bu, F. Song, X. Wan, B. Wang and G. Wang, *Phys. Rev. B*, 2017, **96**, 041201.
39 E. Li, R.-Z. Zhang, H. Li, C. Liu, G. Li, J.-O. Wang, T. Qian, H. Ding, Y.-Y. Zhang, S.-X. Du, X. Lin and H.-J. Gao, *Chin. Phys. B*, 2018, **27**, 086804.
40 L.-H. Zeng, M.-Z. Wang, H. Hu, B. Nie, Y.-Q. Yu, C.-Y. Wu, L. Wang, J.-G. Hu, C. Xie, F.-X. Liang and L.-B. Luo, *ACS Appl. Mater. Interfaces*, 2013, **5**, 9362–9366.
41 E. Wu, D. Wu, C. Jia, Y. Wang, H. Yuan, L. Zeng, T. Xu, Z. Shi, Y. Tian and X. Li, *ACS Photonics*, 2019, **6**, 565–572.
42 L. Luo, D. Wang, C. Xie, J. Hu, X. Zhao and F. Liang, *Adv. Funct. Mater.*, 2019, **29**, 1900849.
43 L. Wang, J. Jie, Z. Shao, Q. Zhang, X. Zhang, Y. Wang, Z. Sun and S.-T. Lee, *Adv. Funct. Mater.*, 2015, **25**, 2910–2919.
44 L.-B. Luo, J.-J. Chen, M.-Z. Wang, H. Hu, C.-Y. Wu, Q. Li, L. Wang, J.-A. Huang and F.-X. Liang, *Adv. Funct. Mater.*, 2014, **24**, 2794–2800.
45 X. An, F. Liu, Y. J. Jung and S. Kar, *Nano Lett.*, 2013, **13**, 909–916.
46 W. Hu, H. Cong, W. Huang, Y. Huang, L. Chen, A. Pan and C. Xue, *Light: Sci. Appl.*, 2019, **8**, 106.
47 F. Zeng, Y. Guo, W. Hu, Y. Tan, X. Zhang, J. Yang, Q. Lin, Y. Peng, X. Tang, Z. Liu, Z. Yao and J. Du, *J. Lumin.*, 2020, **223**, 117178.
48 S. M. Sze and K. K. Ng, *Physics of Semiconductor Devices*, 2007.
49 Y.-Y. Chen, H.-C. Chang, Y.-H. Chi, C.-H. Huang and C. W. Liu, *IEEE Electron Device Lett.*, 2013, **34**, 444–446.
50 W. Song, J. Chen, Z. Li and X. Fang, *Adv. Mater.*, 2021, **33**, 2101059.
51 C. Xie, Y. Wang, Z. X. Zhang, D. Wang and L. B. Luo, *Nano Today*, 2018, **19**, 41–83.
52 X. Wan, Y. Xu, H. Guo, K. Shehzad, A. Ali, Y. Liu, J. Yang, D. Dai, C.-T. Lin, L. Liu, H.-C. Cheng, F. Wang, X. Wang, H. Lu, W. Hu, X. Pi, Y. Dan, J. Luo, T. Hasan, X. Duan, X. Li, J. Xu, D. Yang, T. Ren and B. Yu, *npj 2D Mater. Appl.*, 2017, **1**, 4.
53 R. Lu, C.-W. Ge, Y.-F. Zou, K. Zheng, D.-D. Wang, T.-F. Zhang and L.-B. Luo, *Laser Photonics Rev.*, 2016, **10**, 595–602.
54 L. Wang, J.-J. Li, Q. Fan, Z.-F. Huang, Y.-C. Lu, C. Xie, C.-Y. Wu and L.-B. Luo, *J. Mater. Chem. C*, 2019, **7**, 5019–5027.
55 D. Wu, J. Guo, J. Du, C. Xia, L. Zeng, Y. Tian, Z. Shi, Y. Tian, X. J. Li, Y. H. Tsang and J. Jie, *ACS Nano*, 2019, **13**, 9907–9917.
56 Z. Xu, S. Lin, X. Li, S. Zhang, Z. Wu, W. Xu, Y. Lu and S. Xu, *Nano Energy*, 2016, **23**, 89–96.
57 C. Xie, X.-T. Lu, X.-W. Tong, Z.-X. Zhang, F.-X. Liang, L. Liang, L.-B. Luo and Y.-C. Wu, *Adv. Funct. Mater.*, 2019, **29**, 1806006.